Structural Studies on 3-Hydroxyanthranilate-3,4-dioxygenase: The Catalytic Mechanism of a Complex Oxidation Involved in NAD Biosynthesis[†,‡]

Yang Zhang, Keri L. Colabroy, Tadhg P. Begley,* and Steven E. Ealick*

Department of Chemistry and Chemical Biology, Cornell University, Ithaca, New York 14853

Received December 16, 2004; Revised Manuscript Received March 16, 2005

ABSTRACT: 3-Hydroxyanthranilate-3,4-dioxygenase (HAD) catalyzes the oxidative ring opening of 3-hydroxyanthranilate in the final enzymatic step of the biosynthetic pathway from tryptophan to quinolinate, the universal de novo precursor to the pyridine ring of nicotinamide adenine dinucleotide. The enzyme requires Fe^{2+} as a cofactor and is inactivated by 4-chloro-3-hydroxyanthranilate. HAD from *Ralstonia metallidurans* was crystallized, and the structure was determined at 1.9 Å resolution. The structures of HAD complexed with the inhibitor 4-chloro-3-hydroxyanthranilic acid and either molecular oxygen or nitric oxide were determined at 2.0 Å resolution, and the structure of HAD complexed with 3-hydroxyanthranilate was determined at 3.2 Å resolution. HAD is a homodimer with a subunit topology that is characteristic of the cupin barrel fold. Each monomer contains two iron binding sites. The catalytic iron is buried deep inside the β-barrel with His^{51}, Glu^{57}, and His^{95} serving as ligands. The other iron site forms an FeS_4 center close to the solvent surface in which the sulfur atoms are provided by Cys^{125}, Cys^{128}, Cys^{162}, and Cys^{165}. The two iron sites are separated by 24 Å. On the basis of the crystal structures of HAD, mutagenesis studies were carried out in order to elucidate the enzyme mechanism. In addition, a new mechanism for the enzyme inactivation by 4-chloro-3-hydroxyanthranilate is proposed.

3-Hydroxyanthranilate-3,4-dioxygenase (HAD[1]) catalyzes the oxidative ring opening of 3-hydroxyanthranilate (HAA) to yield 2-amino-3-carboxymuconic semialdehyde (Scheme 1). The reaction is the final enzymatic step in the tryptophan to quinolinate biosynthetic pathway. The biosynthesis of quinolinate from tryptophan is of substantial interest because quinolinate is the precursor to the pyridine ring of the nicotinamide cofactors. Quinolinate also plays an important role in several other biological processes (*1*). As a structural analogue of neurotransmitters such as glutamate and aspartate, quinolinate was shown to selectively activate amino acid receptors such as the *N*-methyl-D-aspartate (NMDA) receptor (*1*−*3*). NMDA receptors have been linked to pathological processes in a variety of central nervous system disorders and to inflammatory conditions, such as Huntington's disease, epilepsy, hepatic encephalopathy, and AIDS-related dementia. Elevated levels of quinolinate in cerebrospinal fluid and serum have been detected with aging and following the immunodeficiency in patients affected by AIDS (*4*, *5*).

Scheme 1: The Reaction Catalyzed by HAD

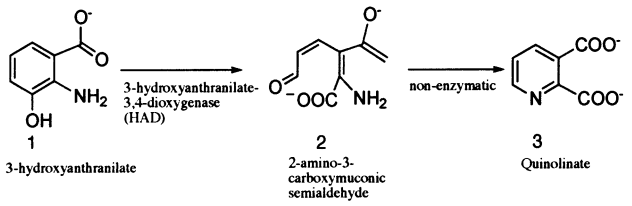

It has been generally believed that the biosynthesis of quinolinate from tryptophan is unique to eukaryotes, while in prokaryotes quinolinate is derived from aspartate and dihydroxyacetone phosphate. However, the tryptophan to quinolinate biosynthetic pathway and HAD activity have been recently identified in several bacteria including *Ralstonia metallidurans* (*6*). HAD from various eukaryotic sources is poorly characterized due to stability and overexpression problems (*7*, *8*). The identification and overexpression of a bacterial HAD from *R. metallidurans* has made this enzyme available in substantial quantities, greatly facilitating structural and mechanistic studies.

HAD is a non-heme Fe^{2+} dependent extradiol dioxygenase. The enzyme from *R. metallidurans* is a homodimer with 174 amino acids per monomer and a molecular weight of 22 kDa/monomer. The enzyme is inactive after purification, but activity can be reconstituted by incubation with Fe^{2+} and DTT. 4-Chloro-3-hydroxyanthranilate (ClHAA) has been identified as a mechanism based inactivating agent. The mechanism of this inactivation is described in the accompanying paper (*9*).

In this paper, we present the crystal structure of unliganded HAD determined at 1.9 Å resolution, the structures of HAD

[†] This work was supported by National Institutes of Health Grants DK44083 (to T.P.B.) and RR15301 (to S.E.E.). S.E.E. is indebted to the W. M. Keck Foundation and the Lucille P. Markey Charitable Trust.

[‡] The Brookhaven Protein Data Bank code for HAD is 1YFU, for the HAD/ClHAA/O_2 complex is 1YFW, for the HAD/ClHAA/NO complex is 1YFX, and for the HAD/HAA complex is 1YFY.

* To whom correspondence should be addressed at the Department of Chemistry and Chemical Biology, Cornell University, Ithaca, NY 14853. Tel: (607) 255-7961. Fax: (607) 255-1227. E-mail: see3@cornell.edu or tbp2@cornell.edu.

[1] Abbreviations: ClHAA, 4-chloro-3-hydroxyanthranilic acid; NMDA, *N*-methyl-D-aspartate; HAA, 3-hydroxyanthranilic acid; HAD, 3-hydroxyanthranilate-3,4-dioxygenase; HGO, homogentisate 1,2-dioxygenase; QDO, quercetin 2,3-dioxygenase; ACMS, 2-amino-3-carboxymuconic semialdehyde; OXO, oxalate oxidase.

10.1021/bi047353l CCC: $30.25
Published on Web 05/03/2005

complexed with ClHAA and either molecular oxygen or NO determined at 2.0 Å, and the structure of HAD complexed with HAA determined at 3.2 Å resolution. These studies show that the HAD monomer topology is characteristic of the cupin barrel fold (*10*). Each monomer contains two iron binding sites: a catalytic site and a rubredoxin-like site of unknown function. These two iron sites are 24 Å apart. The catalytic iron is buried at the center of the cupin barrel and is coordinated by His^{51}, Glu^{57}, and His^{95}. In the HAD−ligand complexes, HAA binds to the catalytic iron as a bidentate ligand while ClHAA binds as a monodentate ligand using the 3-hydroxy group. Several residues in the active site were identified as candidates for ligand binding or catalysis.

EXPERIMENTAL PROCEDURES

Overexpression and Purification of HAD. HAD from *R. metallidurans* was subcloned into the expression vector pET16b, and the resulting plasmid pCLK100 was used to transform *Escherichia coli* B834(DE3). For overexpression of native protein, cells were grown at 37 °C in LB media, while for overexpression of selenomethionine (SeMet) substituted protein, cells were grown in M9 minimal salts supplemented with 100 μg/mL ampicillin, 4% (w/v) glucose, 2 mM $MgSO_4$, 0.1 mM $CaCl_2$, 1% BME vitamin solution (GibcoBRL), 25 μg/mL $FeSO_4 \cdot 7H_2O$, and 40 μg/mL of each of the L-amino acids (L-selenomethionine substituted for L-methionine). When the absorbance reached an OD_{600} of 0.8, the cells were induced with 0.1 mM isopropyl β-D-thiogalactoside (IPTG) for an additional 6 h at 25 °C. The cells were then spun down by centrifugation and stored at −80 °C. The frozen cell pellets were resuspended in ice cold wash buffer (50 mM sodium phosphate, pH 7.0, 300 mM NaCl, 1 mM β-mercaptoethanol, and 10 mM imidazole). The cells were sonicated on ice, and the insoluble material was removed by centrifugation at 18000*g* for 20 min. All subsequent protein purification steps were carried out at 4 °C. The clarified cell extract was applied to a 2−5 mL cobalt immobilized metal affinity column (Clontech) equilibrated with the wash buffer minus imidazole. The column was washed with 50 column volumes of the wash buffer. Polyhistidine tagged HAD was eluted from the column with the wash buffer supplemented with 300 mM imidazole. The fractions containing HAD were combined and activity was reconstituted by incubating the protein in the presence of 10 mM phosphate, 10 mM dithiothreitol, 250 mM imidazole, and 1−2 mM $FeSO_4$, at pH 8 (5−60 min). The purified HAD was then buffer exchanged into 10 mM Tris-HCl, pH 7.6 and 1 mM DTT, and then concentrated to 18−20 mg/mL using 10 kDa cutoff microcon concentrators (Amicon). The purified HAD protein is unstable at freezing temperature and has a half-life of only 2−3 days at 4 °C. Hence freshly purified protein was used for crystallization experiments.

Crystallization of HAD. Crystallization was performed using the hanging drop method at 18 °C with drops containing 1.5 μL of protein solution and 1.5 μL of reservoir solution. HAD was subjected to a series of sparse matrix screens (Hampton Research, Emerald Biostructures) in order to determine initial crystallization conditions. Both SeMet and native HAD protein were crystallized from 20% PEG 8000, 200 mM $MgCl_2$, 1 mM DTT, and 100 mM Tris-HCl, pH 8.5−8.7. Crystals, along with granular precipitates, grew in the shape of thin daggers and reached a maximum size of 300 μm × 80 μm × 80 μm in two weeks. These crystals belong to the space group $P6_522$ with unit cell dimensions of $a = 58.4$ Å and $c = 230.4$ Å. Each asymmetric unit contains one monomer, corresponding to a solvent content of 56% and Matthews coefficient of 2.8 $Å^3$/Da.

Preparation of HAD−Ligand Complexes. In order to obtain the structure of the enzyme bound to the ClHAA inhibitor, native crystals were soaked with ClHAA (∼5 mM) for 20 min in either an O_2 saturated or NO saturated stabilization solution. The stabilization solution used for the soaking experiment is similar to the mother liquor but contains 22% PEG 8000. ClHAA was freshly dissolved in the stabilization solution prior to the soaking experiment due to its instability in solution. The O_2 saturated solution was prepared by an O_2 purge. In addition, O_2 gas was bubbled through the reservoir solution while the HAD native crystal was soaked in a sitting drop of ClHAA−O_2 solution. The NO saturated solution was prepared by adding sodium dithionite and NOC-12, an NO releasing compound, to the stabilization solution after degassing and purging with N_2.

The HAA-complexed crystals were prepared using a procedure similar to that described above. The crystals were soaked for shorter time (∼10 min) with freshly prepared HAA (∼1 mM) soaking solution and diffracted poorly compared to the ClHAA-complexed crystals. In addition, if the soaking time or HAA concentration was increased, the crystals did not diffract. Soaking with both HAA and NO releasing compounds was attempted, but the crystals did not diffract.

X-ray Intensity Measurements. For cryoprotection, the crystals were briefly transferred into a buffer similar to the mother liquor but containing 22% PEG 8000 and 20% glycerol. The crystals were then flash frozen by plunging them into liquid nitrogen. A single wavelength data set from a SeMet HAD crystal was collected at a wavelength selected to maximize $\Delta f''$ of the incorporated selenium. Friedel pairs were measured using inverse beam geometry in 10° wedges. This SeMet data set and ClHAA complexed data sets were collected at beam line 8-BM at the Advanced Photon Source using a Quantum 315 detector. A native data set was collected at beamline A1 at the Cornell High Energy Synchrotron Source using a Quantum 210 detector. Exposure times ranged from 15 to 40 s per frame with each frame covering 0.25−1° of rotation depending on the type of detector used and the mosaicity of the crystal. A total of 20−100° of data were collected for each crystal depending on the beam time constraints and the type of crystal. The HKL2000 suite of programs was used for integration and scaling (*11*). Data processing statistics are summarized in Table 1.

Structure Determination and Refinement. Selenium atom positions were determined using SnB, an iterative direct methods program which uses the Shake-and-Bake algorithm (*12*−*16*). SnB runs yielding correct phases showed clear bimodal distributions of R_{min} values. As there is one methionine residue in the HAD sequence other than the N-terminal methionine, one selenium peak was expected. The single selenium atom position was identified as the highest peak, while the two iron positions were found as weaker peaks. The selenium atom position and iron positions were later confirmed using an anomalous difference map. Single wavelength anomalous diffraction (SAD) phases were cal-

Table 1: Data Collection Statistics[a]

data set	SeMet (peak)	native	ClHAA + O_2	ClHAA + NO	HAA
wavelength (Å)	0.9792	0.9769	0.9778	0.9795	0.9791
resolution (Å)	2.35	1.9	2.0	2.0	3.2
reflections	186051	120376	77260	113771	14695
unique reflns	9819	18779	14085	15530	4404
completeness (%)	92.8 (69.0)	97.1 (82.1)	84.1 (39.8)	91.0 (81.2)	92.3 (66.6)
R_{sym}[b] (%)	9.1 (39.4)	5.1 (36.9)	6.8 (23.4)	7.7 (52.3)	17.8 (36.8)
I/σ	32.4 (3.5)	35.8 (2.7)	22.5 (3.6)	25.9 (2.7)	6.7 (1.9)
multiplicity	18.9 (9.1)	6.4 (4.1)	5.5 (3.6)	6.7 (7.0)	3.6 (3.6)

[a] Values for the highest resolution shell are given in parentheses. [b] $R_{sym} = \sum\sum_i|I_i - \langle I\rangle|/\sum\langle I\rangle$, where $\langle I\rangle$ is the mean intensity of the N reflections with intensities I_i and common indices h,k,l.

Table 2: Refinement Statistics

complex	unliganded	ClHAA + O_2	ClHAA + NO	HAA
resolution (Å)	1.9	2.0	2.0	3.2
total no. of residues	174	174	174	174
no. of water molecules	153	90	82	0
rms deviation from ideal geometry				
bonds (Å)	0.005	0.006	0.006	0.009
angles (deg)	1.3	1.4	1.4	1.6
R factor[a]	0.216	0.234	0.244	0.249
R_{free}[b]	0.240	0.268	0.291	0.306
Ramachandran plot				
most favored regions (%)	88.2	86.1	83.3	70.1
additional allowed regions (%)	11.1	13.2	16.7	28.5
generously allowed regions (%)	0.7	0.7	0	1.4
disallowed regions (%)	0.0	0	0	0
average B factors (Å^2)				
protein residues	36.8	53.2	50.3	48.1
water molecules	48.5	61.6	51.9	
the catalytic iron	34.4	42.7	38.7	28.5
the second iron	41.5	58.9	42.2	49.6
ClHAA/HAA		44.4	38.2	82.4
O_2/NO		57.1	40.5	

[a] R factor $= \sum_{hkl}||F_{obs}| - k|F_{cal}||/\sum_{hkl}|F_{obs}|$, where F_{obs} and F_{cal} are observed and calculated structure factors, respectively. [b] For R_{free} the sum is extended over a subset of reflections (5%) excluded from all stages of refinement.

culated using the selenium atom site and the two iron sites. The phases were improved by density modification using the CNS software package (*17*). The resulting map was readily interpretable, and an initial model was built using the interactive graphics program O (*18*). The model was refined at 2.4 Å resolution by successive cycles of rigid body refinement, simulated annealing, *B*-factor refinement, and manual rebuilding. All 174 residues were built into the model; however, the N-terminus and the C-terminus had weaker density corresponding to their relatively high temperature factors. The resulting model was used to refine against the native data set at 1.9 Å resolution and the ClHAA complexed data sets at 2.0 Å resolution. The ClHAA complexed structures showed a more closed conformation, and the regions with different conformation were manually rebuilt using composite omit maps. The refined model of the closed conformation was used to refine against the HAA complexed data set at 3.2 Å resolution. Models of the bound ligands were directly constructed into the corresponding difference electron densities in the HAD−ligand complexes. Water molecules were included after the ligand model building. Model refinement statistics are summarized in Table 2.

Mutagenesis of R. metallidurans HAD. Standard methods were used for DNA manipulations (*19, 20*). Plasmid DNA was purified with the Qiagen Miniprep kit. *E. coli* strain MachI (Invitrogen) was used as a recipient for transformations during plasmid construction and for plasmid propagation and storage. Site-directed mutagenesis was performed on pRmHAD.16 (pKLC100) (*6*) by a standard PCR protocol using *Pfu*Turbo DNA polymerase according to the manufacturer's instructions (Invitrogen), and *Dpn*I (New England Biolabs) to digest the methylated parental DNA prior to transformation.

R99A. The following complementary primer pair was used: R99AF, 5′-CGC CAT TCC CCG CAG GCC CCC GAG GCC GGC AGC G-3′, and R99AR, 5′-CGC TGC CGG CCT CGG GGG CCT GCG GGG AAT GGC GC-3′. Clones were screened by restriction digest for the introduction of a *Bgl*I site. A representative clone with the correct restriction pattern was sequenced and named pRmHAD.16 R99A.

E110A. The following complementary primer pair was used: E110AF, 5′-GCG CCT GCC TGG TGA TCG CGC GGC AGC GGC CCG CCG G-3′, and E110AR, 5′-CCG GCG GGC CGC TGC CGC GCG ATC ACC AGG CAG GCG C-3′. Clones were screened by restriction digest for the loss of the *Bsr*BI site. A representative clone with the correct restriction pattern was sequenced and named pRmHAD.16 E110A.

R47A. The R47A mutant was difficult to make by the standard plasmid PCR mutagenesis method, so SOE-PCR was used. The vector-specific T7 promoter and T7 terminator primers were used as the outer primer pair, and the mutation was introduced with the following complementary primer pair: R47AF, 5′-GGC GGG CCC AAC CAC GCC ACG GAT TAT CAC GAC G-3′, and R47AR, 5′-CGT CGT GAT AAT CCG TGG CGT GGT TGG GCC CGC C-3′. The mutant gene was excised from the PCR product with *Nde*I and *Bam*HI and ligated into similarly digested pET-16b. Clones were screened for the mutation by restriction digestion with *Btg*I. A representative clone with the correct restriction pattern was sequenced and named pRmHAD.16 R47A.

Overexpression of R. metallidurans HAD Mutants. E. coli strain Tuner(DE3) (Stratagene, La Jolla, CA) was used for protein overexpression. LB medium (5 mL) containing ampicillin (200 μg/mL) was inoculated with a single colony of *E. coli* Tuner(DE3) cells transformed with pRmHAD.16 R99A, pRmHAD.16 E110A, or pRmHAD.16 R47A. The culture was incubated overnight at 37 °C with agitation. On the next day, 1 L of LB media containing 200 μg/mL ampicillin was inoculated with 1.0 mL of the starter culture. The cells were grown with shaking at 37 °C until the culture

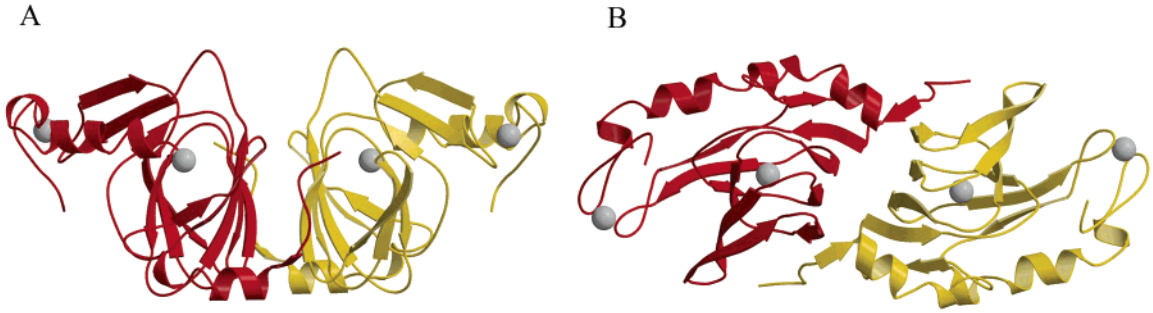

FIGURE 1: Structure of the HAD dimer colored by subunit: (A) a top view down the axis of the β-barrel; (B) a side view parallel to the axis of the β-barrel.

reached an OD_{600} of 0.4. The temperature was then reduced to 25 °C, and the cells were allowed to grow to an OD_{600} of 0.6. IPTG was added to a final concentration of 0.1 mM, and the culture was incubated for an additional 5 h at 25 °C. The cells were then harvested by centrifugation at 8300*g* for 15 min at 4 °C and stored at −20 °C.

Purification and Reconstitution of R. metallidurans HAD Mutants. The frozen cells containing the overexpressed HAD mutants were resuspended in potassium phosphate buffer (50 mM, pH 8) containing sodium chloride (300 mM) and imidazole (10 mM). Lysozyme (0.1 mg/mL) was added, and the cells were sonicated on ice. The cell debris was removed by centrifugation at 27000*g* for 15 min at 4 °C. The supernatant containing the mutant HAD was purified by Ni-NTA affinity chromatography. Ni-NTA superflow resin (1 mL) was equilibrated with 50 mM potassium phosphate buffer (pH 8, 300 mM NaCl, 10 mM imidazole). HAD was bound to the resin (200 μg of protein/mL of resin) and washed with 50 mM potassium phosphate buffer (pH 8, 300 mM NaCl, 20 mM imidazole). HAD was eluted in 1 mL fractions (50 mM potassium phosphate buffer, pH 8, 300 mM NaCl, 250 mM imidazole). Activity was reconstituted as described above for wild-type HAD. The reconstituting agents were then removed by rapid gel filtration using a Bio Spin 6 or an Econo Pac 10DG column, eluting with 10 mM phosphate buffer, pH 7.2.

3-Hydroxyanthranilate-3,4-dioxygenase Assay. The activity of each HAD mutant was measured by monitoring the absorbance increase at 360 nm resulting from the production of 2-amino-3-carboxymuconic semialdehyde as previously described (*6*) (ACMS, $\epsilon_{360} = 47500\ M^{-1}\ cm^{-1}$) (*21*). A typical reaction mixture consisted of 5−100 μM HAA, and 400−600 ng of reconstituted mutant HAD diluted to 500 μL with 10 mM phosphate pH 7.2 buffer. For the determination of kinetic parameters, initial rates of product formation were plotted versus the substrate concentration and fit to the Michaelis−Menten equation using Origin 6.0. The results are described below and summarized in Table 3.

Preparation of Figures. The graphics for figures were prepared using MOLSCRIPT (*22*−*24*) and RASTER3D (*25*) and ChemDraw.

RESULTS

Crystal Structure of R. metallidurans HAD. The final model of HAD contains all 174 residues. Both the N-terminus and the C-terminus are ordered in the structure, although their temperature factors are relatively high in comparison with those of the central region. The overall structure is a dimer with approximate dimensions 80 Å × 40 Å × 30 Å and in which the two monomers are related by a crystallographic 2-fold axis (Figure 1). The core motif of the monomer structure is a jellyroll β-barrel formed by the two antiparallel β-sheets with a topology that is characteristic of the cupin barrel fold (*10*) (Figure 2). In addition, the arrangement of the two cupin barrels in a dimer resembles bicupin structures in which each monomer has two cupin domains (*10*). The two antiparallel β-sheets, 0↑1↓2↑9↓4↑7↓ and 11↓10↑3↓8↑5↓6↑, are both six-stranded. The former β-sheet comprises strands from both monomers, in which β0 comes from one monomer and the remaining five strands from the other. Each of the twelve β-strands is approximately perpendicular to the barrel axis. In addition to the central barrel, the monomer contains three α-helices and a 3_{10} helix. Helix α1 comprises eight residues located at the N-terminal region with the 3_{10} helix located at the C-terminal end. The other two α-helices (α2 and α3) are in the C-terminal region. Surprisingly, helix α2 contains two consecutive proline residues (Pro^{147} and Pro^{148}). These two proline residues are located at the 6th and 7th positions of this thirteen-residue helix and create a bend between the first and second turns. Besides Pro^{147}-Pro^{148}, there are two other pairs of consecutive proline residues in the structure: Pro^{23}-Pro^{24} in the loop connecting the 3_{10} helix and β1, and Pro^{90}-Pro^{91} in the turn between β7 and β8.

Table 3: Apparent Kinetic Parameters for HAD Mutants

	K_m (HAA, μM)	k_{cat} (s^{-1})	$k_{cat}/K_m \times 10^3$ ($s^{-1}\ \mu M^{-1}$)
WT	22.4 ± 2.7	25	1,116
R47A	147.0 ± 14.0	0.022	0.15
R99A	872.0 ± 140	0.0046	0.005
E110A	10.2 ± 1.1	0.012	1.17

The dimer interface, which buries a total surface area of about 3000 $Å^2$, is primarily formed by the six-stranded β-sheet 0↑1↓2↑9↓4↑7↓ from each subunit. These 2-fold related β-sheets form a two-layered sandwich at their outer surface relative to the center of the β-barrel. Other residues composing the contact area come from the N-terminal loop and the N-terminal end of α1. A total of 14 direct hydrogen bonding interactions are found at the edge of the two-layered sandwich between the two monomers. These include two hydrogen bonds between β0 and $\beta7'$, which help form one of the β-sheets of the cupin barrel. The central area of the dimer interface is strictly hydrophobic.

The inner surface of the narrower end of the cupin barrel formed by β5−β7 is mostly hydrophobic, while the remainder of the barrel can be divided into small patches of hydrophobic and hydrophilic areas. A cluster of buried

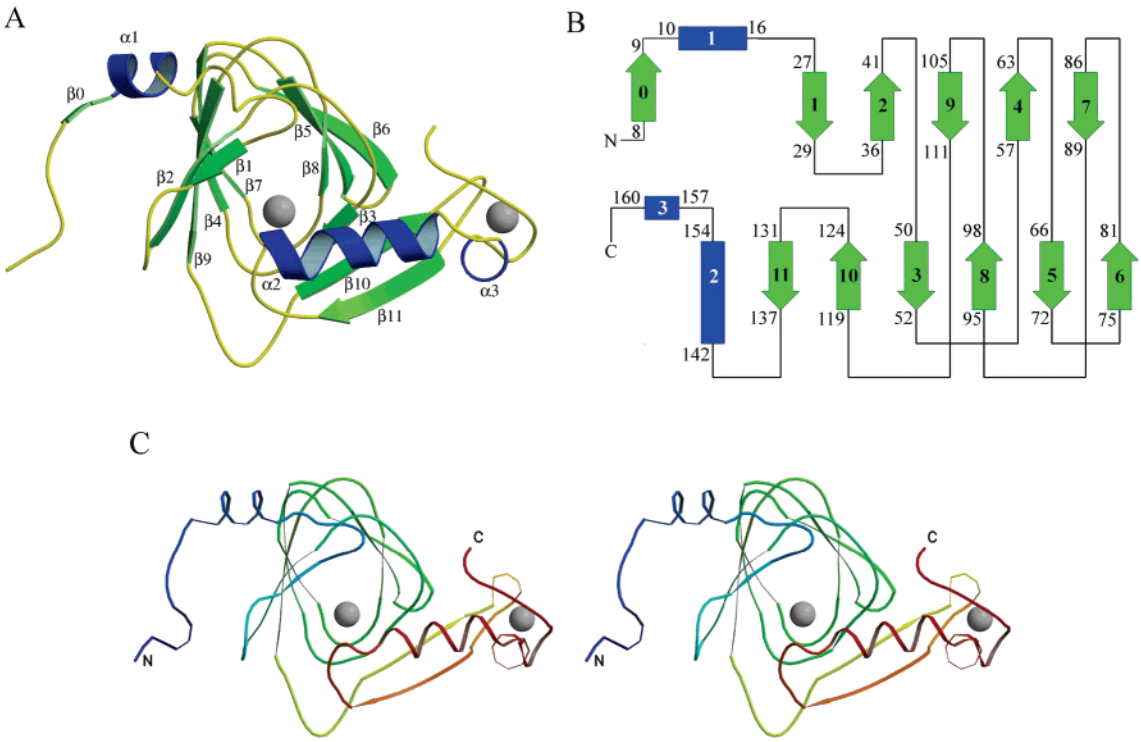

FIGURE 2: Structure of HAD monomer: (A) ribbon diagram colored by secondary structure elements; (B) topology diagram; (C) stereodiagram of the backbone tracing.

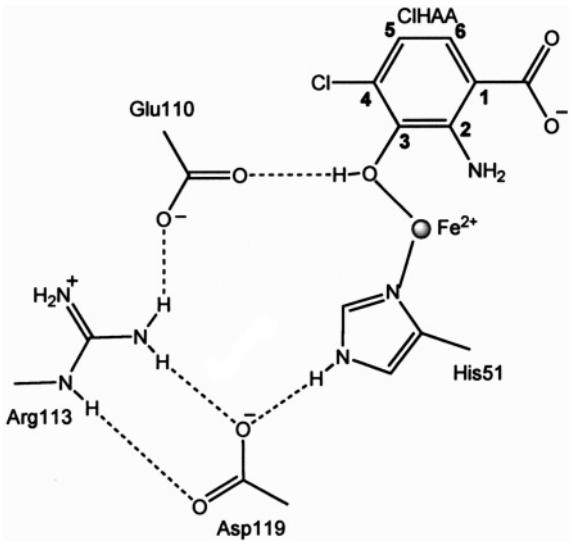

FIGURE 3: The schematic diagram of the hydrogen bonding network in the vicinity of the substrate binding site.

hydrophilic residues, including His[51], Glu[110], Arg[113], and Asp[119], is found at the center of the β-barrel near the active site. The residues form a hydrogen bonding network, with ends that are linked by the catalytic iron (Figure 3).

Active Site Structure of Unliganded HAD. A complete active site, which contains an Fe(II) ion, is found in each HAD monomer and is buried deeply inside the cupin barrel. The Fe(II) ion has a distorted octahedral geometry (Figure 4A). The coordination ligands include two histidine residues (His[51] and His[95]), a bidentate glutamate residue (Glu[57]), and a water molecule. In addition, electron density at the sixth coordination site showed elongated density. This density was modeled as a water molecule because the density for the second atom of a possible oxygen molecule was weak and binding of oxygen in the absence of substrate is not predicted to occur (see accompanying paper (*9*)). The four planar ligands comprise the N^{δ} atom of His[51], two O^{ϵ} atoms of Glu[57], and the oxygen atom of a water molecule. The N^{ϵ} atom of His[95] and an oxygen atom of the other water molecule make the two axial ligands. The coordinate bond distances range from 2.2 to 2.4 Å, except for the Glu[57] $O^{\epsilon 1}$, atom where the distance is 2.7 Å. A chloride anion was found 6.3 Å from the catalytic iron, forming a salt bridge with Arg[99]. The presence of the chloride anion is probably not catalytically relevant but rather is due to the high chloride concentration in the crystallization buffer.

The FeS_4 Center. In addition to the active site, a second iron binding site is found 24 Å away from the catalytic iron atom in each of our structures. This second iron ion is located in the C-terminal region at the periphery of the molecule and is sandwiched between two hairpin loops formed by residues 125−130 and 160−168 (Figure 4E). The second iron ion is coordinated by the sulfur atoms of four highly conserved cysteine residues (Cys[125], Cys[128], Cys[162], and Cys[165]) forming an almost regular tetrahedral FeS_4 center. The coordinate bond distances of the FeS_4 center range from 2.3 to 2.5 Å. A Tris molecule is bound near the FeS_4 center in all of our HAD structures, making hydrogen bonding interactions with the N^{δ} atom of His[133] and the carbonyl groups of Val[132], Asp[158], Lys[159], and Arg[161].

Structure of the Active Site with Ligands Bound. The HAD−ClHAA−O_2 complex and the HAD−ClHAA−NO complex show the same substrate binding interactions. The inhibitor ClHAA was bound at the active site in both structures with clearly visible electron density (Figure 4C). Molecular oxygen and NO were identified as elongated density at the same coordinate location; however, the temperature factors of O_2 are higher than those of NO. In both structures, the catalytic iron coordinates to six ligands,

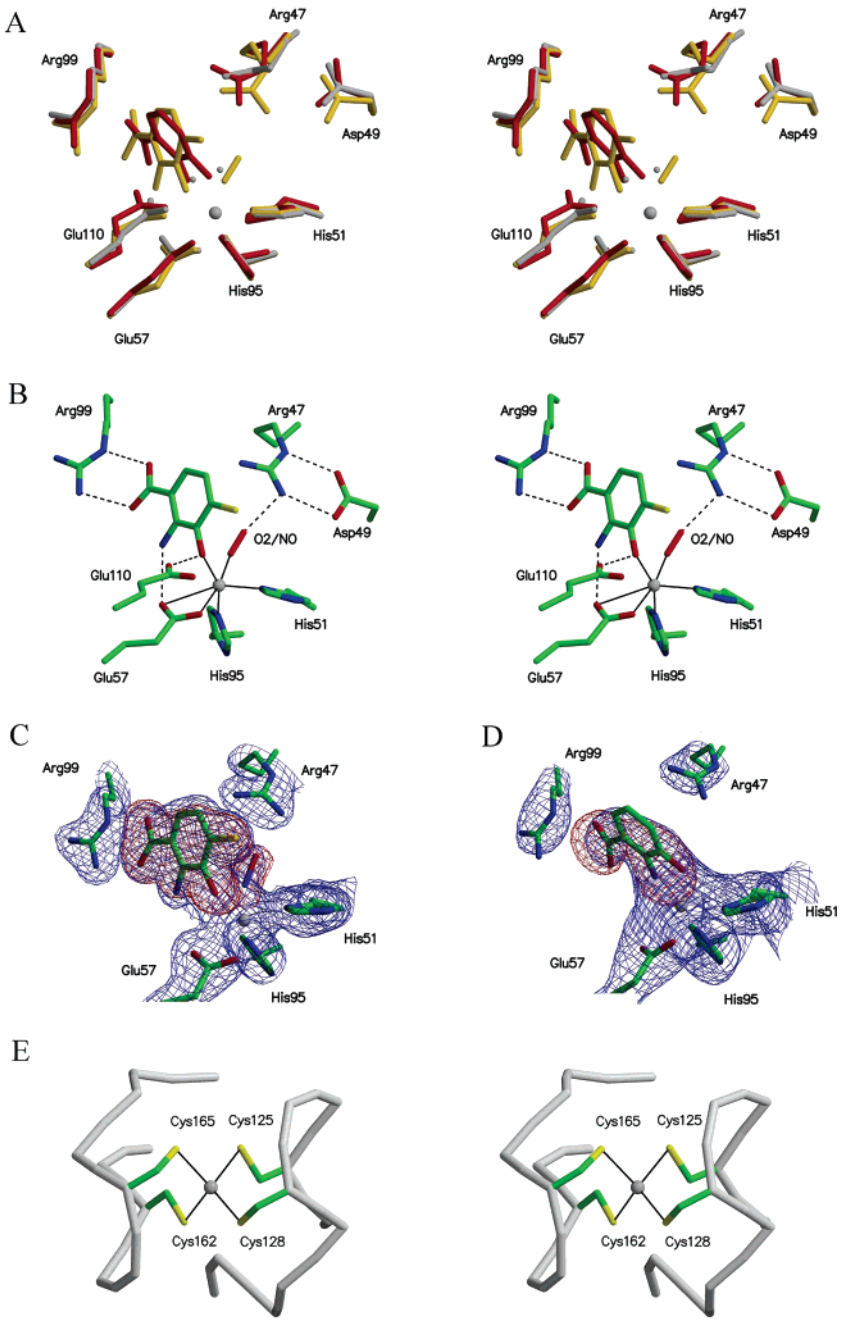

FIGURE 4: The iron binding sites: (A) the superimposed active sites of the unliganded structure (gray), the ClHAA complexed structure (yellow), and the HAA complexed structure (red); (B) a stereodiagram of the active site with ClHAA bound to the catalytic iron; (C) electron density ($F_o - F_c$ map contoured at 3σ in red and $2F_o - F_c$ map contoured at 1σ in blue) corresponding to ClHAA and NO in the active site; (D) electron density ($F_o - F_c$ map contoured at 3σ in red and $2F_o - F_c$ map contoured at 1σ in blue) corresponding to HAA in the active site; (E) the FeS_4 center.

which comprise His^{51}, bidentate Glu^{57}, His^{95}, ClHAA, and an O_2/NO molecule, with a distorted octahedral geometry similar to that found in the unliganded structure (Figure 4B). Of the two axial ligands, one comes from the 3-hydroxy group of ClHAA and the other is the N^{ϵ} atom of His^{95}. The four planar ligands include the N^{δ} atom of His^{51}, the two O^{ϵ} atoms of Glu^{57}, and an oxygen atom of the bound molecular oxygen or the nitrogen atom of NO. The dioxygen molecule of the HAD−ClHAA−O_2 complex and the NO molecule of the HAD−ClHAA−NO complex bind the catalytic iron at the same site. Similar to the unliganded structure, the Fe−$Glu^{57}O^{\epsilon 1}$ bond (2.8 Å) is longer than the Fe−$Glu^{57}O^{\epsilon 2}$ bond and the other coordinate bonds with the iron atom, which range from 2 to 2.3 Å.

The inhibitor ClHAA interacts with the active site Fe(III) via its 3-hydroxy group as a monodentate ligand. The 2-amino group does not interact with the iron atom; rather it forms a hydrogen bond to the O^{ϵ} atom of Glu^{57}. The carboxylate group of ClHAA occupies the position of the chloride anion in the unliganded structure, and forms two hydrogen bonds to Arg^{99}. The 3-hydroxy group of ClHAA also forms a strong hydrogen bond to Glu^{110} with a hydrogen bond distance of 2.4 Å. The hydrophobic face of ClHAA is located in a hydrophobic pocket, which is formed by

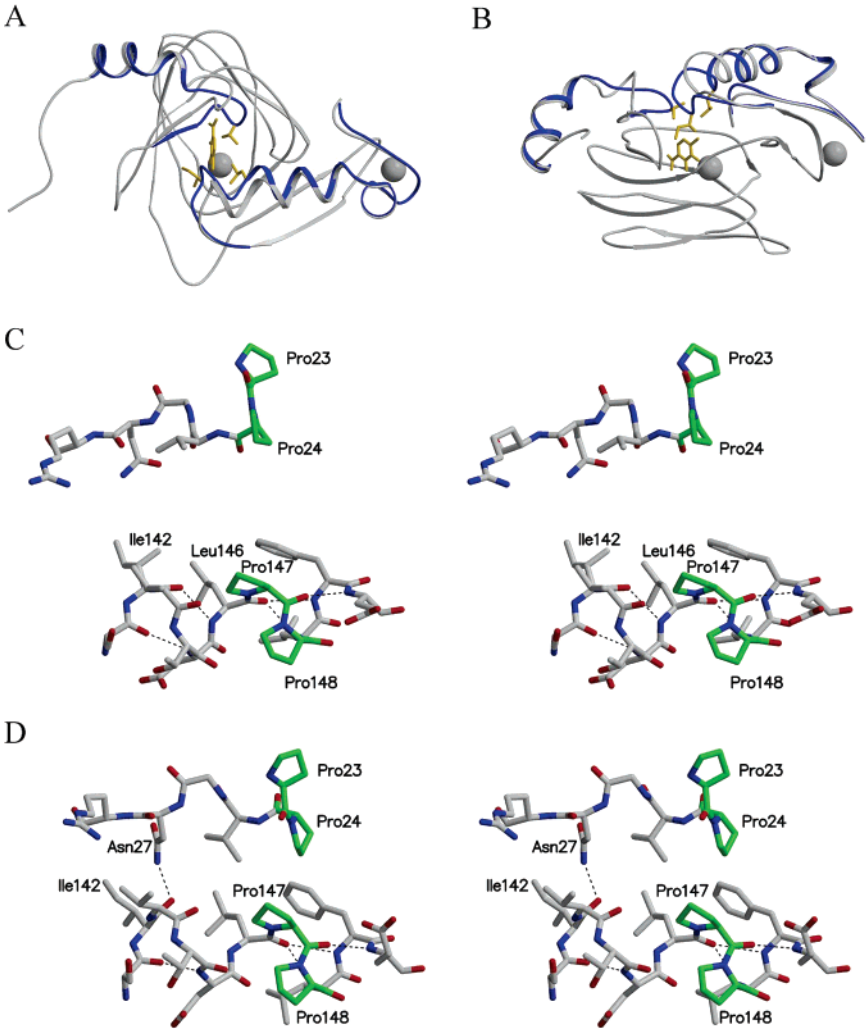

FIGURE 5: The conformational changes upon ligand binding. The unliganded structure and the ClHAA complexed structure are superimposed in panel A as a top view down the axis of the β-barrel and in panel B as a side view parallel to the axis of the β-barrel. Compared to the unliganded structure (gray), β1 and α2 in the ClHAA complexed structure (blue) exhibit a more closed conformation. ClHAA, Val^{25}, Ile^{142}, and Leu^{146} in the closed conformation are shown as ball-and-stick models in yellow. Details of β1 and α2 in the unliganded structure and in the ClHAA liganded structure are shown in panels C and D, respectively. The hydrogen bond between the carbonyl of Ile^{142} and the backbone nitrogen atom of Leu^{146} in the unliganded structure is broken upon ClHAA binding, while a new hydrogen bond is formed between the carbonyl of Ile^{142} and the N^{δ} atom of Asn^{27}. The two pairs of consecutive proline residues are highlighted in green.

conformational changes upon ligand binding. This hydrophobic pocket is primarily formed by Val^{25}, Phe^{121}, Ile^{142}, and Leu^{146}.

Unlike the binding of inhibitor ClHAA, the substrate HAA binds to the iron as a bidentate ligand in the HAD−HAA structure. The benzene ring of HAA also tilts about 30° relative to ClHAA in the HAD−ClHAA structures (Figure 4A). As a consequence, the C-3 carbon atom of the substrate moves closer to the dioxygen binding site than the corresponding carbon of the inhibitor.

The Conformational Changes upon Ligand Binding. The structures of HAD complexed with ClHAA and either molecular oxygen or NO were solved at 2.0 Å resolution. The structure of HAD complexed with HAA was solved at lower resolution (3.2 Å). All three ligand-containing structures exhibit the same tertiary and quaternary structure as the substrate free structure, except that the liganded structures show a more closed active site conformation.

The most significant conformational changes upon ligand binding occur at the terminal regions comprising β1 and α2 (Figure 5). At the N-terminal region, the loop containing residues 21−27 (connecting α1 and β1) and β1 move toward the center of the β-barrel. At the C-terminal region, α2 unwinds one helical turn at its N-terminal end and also moves toward the center of the β-barrel. The two consecutive proline residues of α2 (Pro^{147} and Pro^{148}) become the second and the third residues in this shorter helix. In the unliganded structure, these two proline residues disrupt the normal hydrogen bonding interactions within the α-helix because the carbonyl groups of three residues at the second through fourth positions of α2 (Val^{143}, Thr^{144}, and Asp^{145}) have no hydrogen bonding partners. To unwind the first helical turn, only one hydrogen bond between the carbonyl of Ile^{142} and the backbone nitrogen atom of Leu^{146} needs to be broken. This is compensated for by a new hydrogen bond formed between the carbonyl of Ile^{142} and the N^{δ} atom of Asn^{27}. Therefore, the total number of hydrogen bonds is unchanged upon the unwinding of the first turn of α2 and hydrophobic interactions appear to be the driving force for the conformational changes. As a result of this closing movement, the

side chains of three hydrophobic residues (Val[25], Ile[142], and Leu[146]) move toward the active site and together with Phe[121] form a hydrophobic pocket for ligand binding.

In addition to the residues forming the hydrophobic pocket, two hydrophilic residues show significant conformational changes that help accommodate the O_2/NO molecule bound to the catalytic iron. The guanidinium group of Arg[47] moves about 0.9 Å toward the catalytic iron and makes a hydrogen bond to the bound oxygen (or NO), while Asp[49] moves about 0.7 Å so as to maintain two hydrogen bonds with Arg[47]. The other residues in the vicinity of the active site remain essentially in the same positions as in the unliganded structure. This includes the hydrogen bond network consisting of His[51], Glu[110], Arg[113], and Asp[119].

Activity of HAD Mutants. The apparent catalytic activity of all mutants was determined by measuring the rate of product formation at 360 nm ($\epsilon = 47500\ M^{-1}\ cm^{-1}$ for **2**). The K_m and V_{max} for each mutant were determined by fitting the rate of product formation versus substrate concentration to the Michaelis−Menten equation using Origin 6.0; the results are shown in Table 3. The R47A mutant showed substrate inhibition; therefore, its kinetic constants were determined from a fit to the substrate inhibition equation ($K_i = 2.5 \pm 0.3$ mM).

DISCUSSION

Quality of the X-ray Intensity Data and Structures. The structure of unliganded HAD was determined at 1.9 Å resolution. The structures of HAD complexed with the inhibitor ClHAA and either O_2 or NO were determined at 2.0 Å resolution, and the structure of HAD complexed with 3-hydroxyanthranilate was determined at 3.2 Å resolution. The final electron density maps were clear and reasonable for the stated resolution. All three complexes have relatively high *B* factors and *R* factors, which are probably related to crystal quality. Crystals could only be obtained from freshly prepared protein and showed anisotropic diffraction. Consequently all the datasets have low completeness in the highest resolution shell and the refinements gave slightly higher *R* factors than would be expected for 1.9−2.0 Å resolution. The inhibitor ClHAA showed clear density in both HAD−ClHAA−O_2 and HAD−ClHAA−NO complexes (Figure 4C). The data quality of the HAA complex is much poorer compared to the other data sets. The crystal complexed with HAA diffracted only to 3.2 Å resolution and had high mosaicity (∼1.5). HAA showed slightly weaker electron density for the C-4, C-5, and C-6 atoms (Figure 4D); however, the orientation and position of the ligand were unambiguous.

Comparison of HAD with Other Cupin Structures. The HAD structure belongs to the cupin superfamily, which shares a common architecture usually being described as "double-stranded β-helix" or "jelly-roll β-barrel" (*26*). The name cupin came from the Latin name *cupa* for a small barrel. The cupin superfamily contains a group of functionally divergent proteins, including both enzymes and nonenzymes, and is found throughout the Archaea, Eubacteria, and Eukaryota. Members of this superfamily share two histidine containing sequence motifs (*27, 28*) that identify the binding site of the metal, which is usually a first row transition metal ion. HAD has little sequence homology to other superfamily members; however, the overall topology and the active site are structurally conserved. In addition, the dimeric assembly of HAD resembles bicupin structures (e.g., canavalin and oxalate decarboxylase, which were thought to arise through duplication of the monocupin structure) (*27, 29*). A search for structural homologues using DALI revealed fourteen cupin structures including dioxygenases, oxidoreductases/oxygenases, isomerases, seed proteins, and regulatory proteins (Table 4). On the basis of a DALI search, canavalin (*30*) and proglycinin (*31*) are structurally most similar to HAD with *Z* scores of 8.3 and 7.3, respectively. Canavalin and glycinin are seed storage proteins and do not contain a metal binding site. The three-dimensional structural alignment of HAD with these proteins gives an rms deviation of 3.8 Å (121 residues) for canavalin and 3.9 Å (132 residues) for glycinin.

Table 4: Comparison of HAD with Known Protein Structures Using DALI[a]

protein	*Z*[b]	rmsd[c]	LALI[d]	LSEQ2[e]	% IDE[f]
canavalin	8.3	3.8	121	178	17
glycinin	7.3	3.9	132	371	11
quercetin 2,3-dioxygenase	7.1	3.1	111	334	15
oxalate decarboxylase	6.8	3.3	105	377	19
oxalate oxidase	6.8	3.5	123	201	12
glucose-6-phosphate isomerase	6.7	3.1	112	183	13
proline 3-hydroxylase	6.0	3.8	101	260	12
mannose-6-phosphate isomerase	5.9	3.1	109	312	12
homogentisate 1,2-dioxygenase	5.6	3.6	119	419	8
RmLC (epimerase)	5.3	3.1	97	183	11
hypoxia-inducible factor 1	4.5	4.2	105	335	14
deacetoxycephalosporin C synthase	4.3	3.5	103	279	13
isopenicillin N Synthase	4.2	3.3	111	329	13
regulatory protein AraC	4.0	4.3	79	161	15

[a] Structures with unknown function or *Z* score below 4.0 are not included. [b] *Z*, strength of structural similarity in standard deviations above expected. [c] rmsd, root-mean-square deviation. [d] LALI, length of aligned residues. [e] LSEQ2, length of the complete sequence. [f] % IDE, percentage of identical residues.

Quercetin 2,3-dioxygenase (QDO) (*32, 33*) and homogentisate 1,2-dioxygenase (HGO) (*34*) are dioxygenases with cupin folds. QDO is the next most similar structure to HAD with a *Z* score of 7.1, while HGO has a *Z* score of 5.6. QDO is dimeric; however, the QDO monomer has a bicupin structure internally. In addition, QDO has only one metal binding center per monomer and utilizes a copper ion, which is coordinated by three histidine residues and a glutamate residue. HGO is a hexamer, in which each monomer has two domains, an N-terminal cupin domain and a C-terminal α/β domain that resembles a partially formed cupin fold. Unlike the rest of the cupin members, the non-heme iron center of HGO is located at the center of the C-terminal partial cupin instead of at the center of the N-terminal cupin barrel. The iron is coordinated by two histidine residues and a glutamate residue.

Five oxidoreductases/oxygenases are found to be structurally similar to HAD: oxalate oxidase (OXO) (*35*), proline 3-hydroxylase (*36*), hypoxia-inducible factor 1 (*37*), deacetoxycephalosporin C synthase (*38*), and isopenicillin N synthase (*39*). Each enzyme except OXO has a non-heme ferrous iron at the center of the cupin barrel, coordinated by two histidine residues and an aspartate residue. OXO is a manganese containing enzyme, and the metal is bound by three histidine residues and a glutamate. OXO is also reported to have a manganese superoxide dismutase activity (*35*).

Key Active Site Residues. ClHAA is an oxygen dependent mechanism-based inactivator of HAD (*9*). The structures of HAD described here provide molecular snapshots of the free and ligand complexed forms of the enzyme. The active site residues can be divided into three groups: iron binding residues, substrate binding residues, and oxygen binding residues. All of the active site residues, which are fully conserved through all HADs, will be discussed separately below. The iron binding residues include two histidine residues (His^{51} and His^{95}) and a carboxylate (Glu^{57}), which are conserved in sequence among the cupin dioxygenases and located in similar spatial arrangements. Unlike the other dioxygenases, however, Glu^{57} of HAD functions as a bidentate ligand, although the Fe−$Glu^{57}O^{\epsilon 1}$ bond (2.8 Å) is longer than a typical iron−oxygen covalent bond.

The substrate-binding cavity is mostly lined with hydrophobic residues, except for Asn^{27}, Arg^{99}, and Glu^{110}. Asn^{27} is structurally and functionally important, forming a new hydrogen bond with Ile^{142} in the closed conformation upon ligand binding. Arg^{99} is primarily responsible for anchoring the carboxylate group of ClHAA. Consistent with this, the R99A mutant shows a 39-fold increase in the K_m for HAA oxidation (Table 3). Glu^{110} forms a hydrogen bond with the 3-hydroxy of ClHAA. This interaction is important for catalysis; the E110A mutant shows a 2083-fold reduction in k_{cat} (Table 3).

An O_2/NO molecule is bound together with ClHAA in the complexed structures. The dioxygen molecule in the HAD−ClHAA−O_2 complex binds directly to the Fe ion at the same site of the octahedral coordination sphere as NO in the HAD−ClHAA−NO complex. The O_2 binding cavity is lined with a mixture of hydrophobic and hydrophilic residues; the hydrogen bonding appears to be the primary factor for the dioxygen binding. The O_2 is sandwiched between the Fe ion, which provides an end-on Fe−O bond, with a bond distance of 2.0 Å, and the guanidinium group of Arg^{47}, which moves toward the noncovalently bounded oxygen atom to form a hydrogen bond upon the ligand binding. The iron-bound oxygen atom is 2.9 Å from the 3-carbon of ClHAA. The distance between the other oxygen atom and the 3-carbon of ClHAA is 3.5 Å. The catalytic significance of Arg^{47} for oxygen binding is supported by mutagenesis studies in which the R47A mutant showed a 1136-fold reduction in k_{cat}.

The Role of the FeS_4 Center. The rubredoxins (RD) are small monomeric proteins (5−6 kDa) that function as electron carriers (*40*). Several structures have been characterized: desulforedoxin (DX) (*41*, *42*), desulfoferrodoxin (DFX), superoxide reductase (SOR) (*43*), rubrerythrin (RR), and rubrerythrin-like proteins (*44*−*48*). All of these proteins contain a mononuclear iron center in which the iron is ligated to four cysteine residues in a tetrahedral coordination sphere. The four cysteine residues are grouped in pairs and located at two conserved β hairpin motifs. In the cases of RD, HAD, and RR, both pairs of iron ligating cysteine residues are separated by two residues (Cys-X-X-Cys) and consequently the iron is coordinated in a symmetrical tetrahedral ligand environment. For DX, DFX, and SOR the iron is ligated by two cysteine residues from a Cys-X-X-Cys motif and two from a Cys-Cys motif resulting in a slightly distorted tetrahedral coordination environment.

RD and DX are the simplest proteins containing the rubredoxin-like site, with a single FeS_4 center per polypeptide chain, while RR, DFX, and SOR are larger proteins with more than one metal center. RR has been reported to have diverse activities such as pyrophosphatase, superoxide dismutase, and ferrooxidase activities (*46*). DFX has been reported to have superoxide dismutase activity and might play a role in the electron transfer chain in sulfate reducing bacteria (*49*, *50*). SOR is involved in the cellular defense mechanism to eliminate superoxide anion radical in sulfate-reducing and microaerophilic bacteria (*51*). DFX from *Desulfovibrio desulfuricans* and SOR from *Desulfoarculus baarsii* (*43*) are structurally homologous, with an N-terminal domain containing a rubredoxin-like iron center and a C-terminal catalytic domain containing a mononuclear iron center. The structure of RR from *Desulfovibrio vulgaris* revealed a C-terminal rubredoxin-like domain and a four-helix bundle surrounding a binuclear metal center in the N-terminal domain.

It has not yet been possible to determine if the rubredoxin-like center in HAD, RR, DFX, and SOR has a redox function or simply plays a structural role. It has been proposed that reduction of Fe(III) at the active site of SOR is achieved by a long range (22 Å) electron transfer from the rubredoxin-like domain (*51*). To test this, the rubredoxin-like site was removed by mutagenesis and the resulting enzyme was still catalytically active. However, as the authors of that study point out, the enzymatic assays were run using a nonphysiological electron donor and therefore do not exclude the possibility of a redox role for the SOR rubredoxin-like site in vivo (*52*). It is also possible that the rubredoxin-like site is not essential as it is absent in *Pyrococcus furiosus* SOR (*53*). For HAD, it is still unclear whether the rubredoxin-like site plays a structural or a redox role. This redox role might involve the reactivation of oxidized enzyme. The four iron ligating cysteine residues of the rubredoxin-like site of HAD are fully conserved throughout bacteria and yeast, but not in other higher organisms. Our efforts to remove this site by mutating the cysteine ligands gave inclusion bodies.

Mechanism of Inhibition by ClHAA. The mechanistic studies described in the companion paper demonstrate that treatment of HAD with ClHAA efficiently inactivates the enzyme (*9*). This inactivation results in the oxidation of the active site from Fe(II) to Fe(III), the consumption of oxygen, and the production of superoxide, suggesting that the enzyme inhibitor complex is unable to proceed to products either because the electron withdrawing chloro substituent makes the electron transfer from the substrate to Fe(III) more difficult or because the chloro substituent inhibits catalysis by perturbing the binding of the substrate. The structures described here enable us to differentiate between these two possibilities. The enzyme/inhibitor/oxygen complex and the enzyme/inhibitor/NO complex both show that the inhibitor binding to the metal ion is monodentate with the phenolic oxygen bound to the metal ion. The monodentate ligation of the inhibitor stands in contrast to all structurally characterized extradiol dioxygenases in which the substrate always functions as a bidentate ligand. In addition, the distance between the terminal oxygen of the iron bound superoxide in the proposed mechanism and the C3 carbon atom of the inhibitor is too long for easy C−O bond formation to give the Criegee intermediate **7** (3.27 Å in the NO complex).

Scheme 2: The Enzyme Inhibitor Complex and the Enzyme Substrate Complex

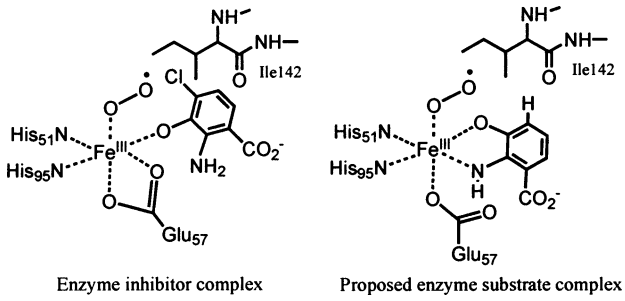

These observations suggest that an unfavorable steric interaction between Ile[142] and the chloro substituent prevents the interaction between the substrate amino group and the active site iron, thus preventing the terminal oxygen atom of an iron bound superoxide from coming within bonding distance of the C3 atom of the substrate (Scheme 2).

Proposed Catalytic Mechanism. On the basis of previous structural and mechanistic studies on extradiol dioxygenases (*54*−*57*), we can propose the mechanism for HAD outlined in Scheme 3. In this mechanism, the substrate binds to the active site Fe(II) by displacing one water molecule and the carbonyl oxygen of Glu[57]. This is followed by oxygen binding and an electron transfer from Fe(II) to oxygen to give **5**. Electron transfer from the electron rich aminophenol to the Fe(III) then gives the diradical **6**. Radical recombination would give peroxide **7** followed by a Criegee rearrangement to give lactone **8**. Hydrolysis of lactone **8** would then give **10**, which dissociates from the enzyme. We have previously demonstrated that the conversion of **2** to **3** is nonenzymatic (*58*). This proposal is supported by mechanistic studies on catechol dioxygenase which provide support for the semiquinone radical, the peroxide, and the lactone intermediates (*59*−*61*). In addition, isotope labeling experiments suggest that the lactone hydrolysis is mediated by the iron−bound oxygen (*62*).

The geometry of the enzyme/inhibitor/oxygen complex allows formation of the proposed superoxide containing intermediate, but the perturbation of the active site geometry by the chloro substituent prevents conversion to product. The structure suggests that the carboxylate group of the substrate interacts with Arg[99]. Consistent with this, the R99A mutant shows a 39-fold increase in the K_m for HAA oxidation. The structure also suggests that the superoxide in intermediate **6** is hydrogen bonded to Arg[47]. This interaction is likely to facilitate oxygen binding and reduction, a role that is supported by the observed 1136-fold reduction in k_{cat} for the R47A mutant. ESR studies on the inhibition of the enzyme with ClHAA demonstrate that oxidation of the active site Fe(II) requires the presence of the inhibitor. Since there are no major structural differences between the free enzyme and the enzyme inhibitor complex in the vicinity of the active site iron, it is likely that binding of the electron rich aminophenol to the active site iron is the event that triggers oxygen reduction. Glu[110] is likely to be involved in phenol deprotonation; this facilitates the electron transfer from the aminophenol to the Fe(III) (**5** to **6**). Phenol deprotonation also facilitates the bond migration that occurs during the Criegee rearrangement (**7** to **8**). Consistent with this, the E110A mutant results in a 2083-fold reduction in k_{cat}. An analogous phenol deprotonation has been observed for catechol dioxygenase (*63*). The migrating bond in the Criegee rearrangement is trans periplanar to the fragmenting O−O bond, the ideal geometry for this rearrangement (*64*). It has been previously proposed that the Criegee rearrangement is acid catalyzed (*65*, *66*). However, we are unable to identify any active site acid interacting with the iron bound peroxide oxygen. This oxygen is therefore highly activated for addition to the lactone carbonyl group to give **9**. In the HAD structure there is a water molecule positioned close to C6 of the lactone. However, it is unlikely that this adds to the lactone because it is not activated by any basic residue. The initially formed product has the cis geometry about the 4,5 double bond; the isolated product has the trans geometry (*58*). While we have not yet determined if this isomerization is enzyme-catalyzed, the structure shows that there is sufficient space for it to occur at the active site. In contrast, isomerization

Scheme 3: Mechanistic Proposal for the HAD Catalyzed Oxidation of 3-Hydroxyanthranilic Acid to 2-Amino-3-carboxymuconic Acid Semialdehyde

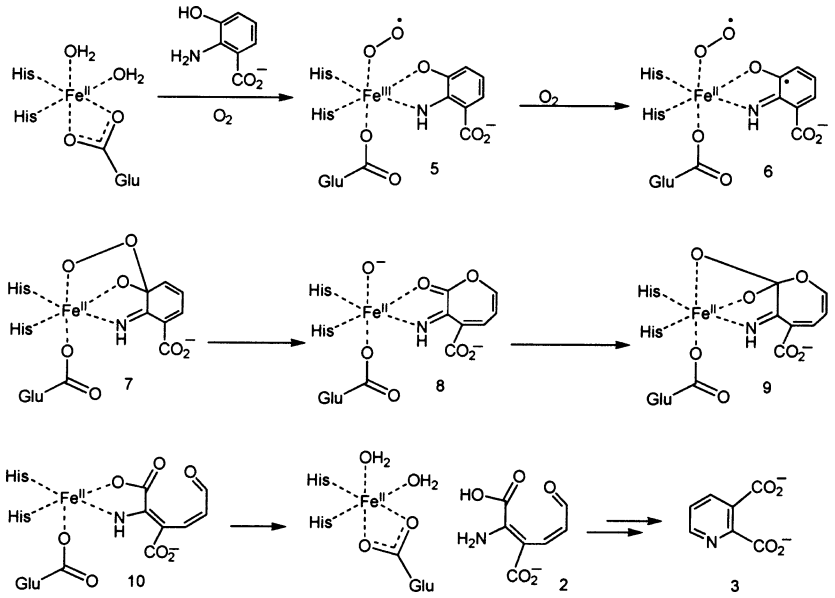

about the C2,3 double bond requires disrupting the interaction between the C3 carboxylate and Arg[99]. Therefore, it is likely that the trans geometry about this double bond is favored in the bound form of the product and that isomerization about this double bond, which is required for quinolinate formation, occurs after product dissociation from the enzyme.

ACKNOWLEDGMENT

We thank Leslie Kinsland for assistance in the preparation of this manuscript. We thank NE-CAT beam line 8-BM, supported by NIH Grant RR15301, and the Cornell High Energy Synchrotron Source for provision of beam time. We thank Cynthia Kinsland for the preparation of the HAD overexpression plasmid and mutants.

REFERENCES

1. Stone, T. W., and Darlington, L. G. (2002) Endogenous kynurenines as targets for drug discovery and development, *Nat. Rev. Drug Discov. 1*, 609−20.
2. Stone, T. W., and Perkins, M. N. (1981) Quinolinic acid: a potent endogenous excitant at amino acid receptors in CNS, *Eur. J. Pharmacol. 72*, 411−2.
3. Schwarcz, R., Whetsell, W. O., Jr., and Mangano, R. M. (1983) Quinolinic acid: an endogenous metabolite that produces axon-sparing lesions in rat brain, *Science 219*, 316−8.
4. Heyes, M. P., Saito, K., Jacobowitz, D., Markey, S. P., Takikawa, O., and Vickers, J. H. (1992) Poliovirus induces indoleamine-2,3-dioxygenase and quinolinic acid synthesis in macaque brain, *FASEB J. 6*, 2977−89.
5. Halperin, J. J., and Heyes, M. P. (1992) Neuroactive kynurenines in Lyme borreliosis, *Neurology 42*, 43−50.
6. Kurnasov, O., Goral, V., Colabroy, K., Gerdes, S., Anantha, S., Osterman, A., and Begley, T. P. (2003) NAD biosynthesis: identification of the tryptophan to quinolinate pathway in bacteria, *Chem. Biol. 10*, 1195−204.
7. Malherbe, P., Koehler, C., Da Prada, M., Lang, G., Kiefer, V., Schwarcz, R., Lahm, H.-W., and Cesura, A. M. (1994) Molecular cloning and functional expression of human 3-hydroxyanthranilic-acid dioxygenase, *J. Biol. Chem. 269*, 13792−7.
8. Koontz, W., and Shiman, R. (1976) Beef Kidney 3-Hydroxy-anthranilic Acid Oxygenase, *J. Biol. Chem. 251*, 368−377.
9. Colabroy, K. L., Zhai, H., Li, T., Ge, Y., Zhang, Y., Liu, A., Ealick, S. E., McLafferty, F. W., and Begley, T. P. (2005) The Mechanism of Inactivation of 3-Hydroxyanthranilate-3,4-dioxygenase by 4-Chloro-3-hydroxyanthranilate, *Biochemistry 44*, 7623−7631.
10. Dunwell, J. M., Purvis, A., and Khuri, S. (2004) Cupins: the most functionally diverse protein superfamily?, *Phytochemistry 65*, 7−17.
11. Otwinowski, Z., and Minor, W. (1997) Processing of x-ray diffraction data collected in oscillation mode, *Methods Enzymol. 276*, 307−326.
12. Smith, G. D., Nagar, B., Rini, J. M., Hauptman, H. A., and Blessing, R. H. (1998) The use of SnB to determine an anomalous scattering substructure, *Acta Crystallogr. D 54*, 799−804.
13. Weeks, C. M., and Miller, R. (1997) SnB: Applying Shake-and-Bake to proteins, in *Proceedings of the Macromolecular Crystallography Computing School* (Watenpaugh, K., Ed.) pp 138−147, International Union of Crystallography, Chester, U.K.
14. Hauptman, H. A. (1991) A minimal principle in the phase problem, in *Crystallographic computing 5: From Chemistry to Biology* (Thierry, J. C., Ed.) pp 324−332, IUCr and Oxford University Press, Oxford, U.K.
15. Miller, R., DeTitta, G. T., Jones, R., Langs, D. A., Weeks, C. M., and Hauptman, H. A. (1993) On the application of the minimal principle to solve unknown structures, *Science 259*, 1430−3.
16. Miller, R., Gallo, S. M., Khalak, H. G., and Weeks, C. M. (1994) SnB: crystal structure determination via shake-and-bake, *J. Appl. Crystallogr. 27*, 613-21.
17. Brünger, A. T., Adams, P. D., Clore, G. M., DeLano, W. L., Gros, P., Grosse-Kunstleve, R. W., Jiang, J. S., Kuszewski, J., Nilges, M., Pannu, N. S., Read, R. J., Rice, L. M., Simonson, T., and Warren, G. L. (1998) Crystallography & NMR system: A new software suite for macromolecular structure determination, *Acta Crystallogr. D 54*, 905−21.
18. Jones, T. A., Zou, J.-Y., Cowan, S. W., and Kjeldgaard, M. (1991) Improved methods for the building of protein models in electron density maps and the location of errors in these models, *Acta Crystallogr. A 47*, 110−9.
19. Ausubel, F. M., and Brent, F. (1987) *Current Protocols in Molecular Biology*, John Wiley and Sons, New York.
20. Sambrook, J., and Fritsch, E. F. (1989) *Molecular Cloning: A Laboratory Manual*, Cold Spring Harbor Laboratory Press, Plainview, NY.
21. Koontz, W., and Shiman, R. (1976) Beef Kidney 3-Hydroxy-anthranilic Acid Oxygenase, *J. Biol. Chem. 251*, 368−77.
22. Esnouf, R. M. (1999) Further additions to MolScript version 1.4, including reading and contouring of electron-density maps, *Acta Crystallogr. D 55*, 938−40.
23. Esnouf, R. (1997) An extensively modified version of Molscript which includes greatly enhanced colouring capabilities, *J. Mol. Graphics 15*, 132−4.
24. Kraulis, P. J. (1991) MOLSCRIPT: a program to produce both detailed and schematic plots of protein structures., *J. Appl. Crystallogr. 24*, 946−50.
25. Merritt, E. A., and Bacon, D. J. (1997) Raster3D: Photorealistic Molecular Graphics, *Methods Enzymol. 277*, 505−24.
26. Dunwell, J. M. (1998) Cupins: a new superfamily of functionally diverse proteins that include germins and plant storage proteins, *Biotechnol. Genet. Eng. Rev. 15*, 1−32.
27. Dunwell, J. M., and Gane, P. J. (1998) Microbial relatives of seed storage proteins: conservation of motifs in a functionally diverse superfamily of enzymes, *J. Mol. Evol. 46*, 147−54.
28. Dunwell, J. M., Khuri, S., and Gane, P. J. (2000) Microbial relatives of the seed storage proteins of higher plants: conservation of structure and diversification of function during evolution of the cupin superfamily, *Microbiol. Mol. Biol. Rev. 64*, 153−79.
29. Anand, R., Dorrestein, P. C., Kinsland, C., Begley, T. P., and Ealick, S. E. (2002) Structure of oxalate decarboxylase from *Bacillus subtilis* at 1.75 Å resolution, *Biochemistry 41*, 7659−69.
30. Ko, T. P., Ng, J. D., and McPherson, A. (1993) The three-dimensional structure of canavalin from jack bean (*Canavalia ensiformis*), *Plant Physiol. 101*, 729−44.
31. Adachi, M., Takenaka, Y., Gidamis, A. B., Mikami, B., and Utsumi, S. (2001) Crystal structure of soybean proglycinin A1aB1b homotrimer, *J. Mol. Biol. 305*, 291−305.
32. Fusetti, F., Schroter, K. H., Steiner, R. A., van Noort, P. I., Pijning, T., Rozeboom, H. J., Kalk, K. H., Egmond, M. R., and Dijkstra, B. W. (2002) Crystal structure of the copper-containing quercetin 2,3-dioxygenase from *Aspergillus japonicus*, *Structure 10*, 259−68.
33. Steiner, R. A., Kooter, I. M., and Dijkstra, B. W. (2002) Functional analysis of the copper-dependent quercetin 2,3-dioxygenase. 1. Ligand-induced coordination changes probed by X-ray crystallography: inhibition, ordering effect, and mechanistic insights, *Biochemistry 41*, 7955−62.
34. Titus, G. P., Mueller, H. A., Burgner, J., Rodriguez De Cordoba, S., Penalva, M. A., and Timm, D. E. (2000) Crystal structure of human homogentisate dioxygenase, *Nat. Struct. Biol. 7*, 542−6.
35. Woo, E. J., Dunwell, J. M., Goodenough, P. W., Marvier, A. C., and Pickersgill, R. W. (2000) Germin is a manganese containing homohexamer with oxalate oxidase and superoxide dismutase activities, *Nat. Struct. Biol. 7*, 1036−40.
36. Clifton, I. J., Hsueh, L. C., Baldwin, J. E., Harlos, K., and Schofield, C. J. (2001) Structure of proline 3-hydroxylase. Evolution of the family of 2-oxoglutarate dependent oxygenases, *Eur. J. Biochem. 268*, 6625−36.
37. Dann, C. E., 3rd, Bruick, R. K., and Deisenhofer, J. (2002) Structure of factor-inhibiting hypoxia-inducible factor 1: An asparaginyl hydroxylase involved in the hypoxic response pathway, *Proc. Natl. Acad. Sci. U.S.A. 99*, 15351−6.
38. Valegard, K., van Scheltinga, A. C., Lloyd, M. D., Hara, T., Ramaswamy, S., Perrakis, A., Thompson, A., Lee, H. J., Baldwin, J. E., Schofield, C. J., Hajdu, J., and Andersson, I. (1998) Structure of a cephalosporin synthase, *Nature 394*, 805−9.
39. Roach, P. L., Clifton, I. J., Fulop, V., Harlos, K., Barton, G. J., Hajdu, J., Andersson, I., Schofield, C. J., and Baldwin, J. E. (1995) Crystal structure of isopenicillin N synthase is the first from a new structural family of enzymes, *Nature 375*, 700−4.
40. Sieker, L. C., Stenkamp, R. E., and LeGall, J. (1994) Rubredoxin in crystalline state, *Methods Enzymol. 243*, 203−16.

41. Archer, M., Huber, R., Tavares, P., Moura, I., Moura, J. J., Carrondo, M. A., Sieker, L. C., LeGall, J., and Romao, M. J. (1995) Crystal structure of desulforedoxin from *Desulfovibrio gigas* determined at 1.8 Å resolution: a novel non-heme iron protein structure, *J. Mol. Biol. 251*, 690−702.
42. Archer, M., Carvalho, A. L., Teixeira, S., Moura, I., Moura, J. J., Rusnak, F., and Romao, M. J. (1999) Structural studies by X-ray diffraction on metal substituted desulforedoxin, a rubredoxin-type protein, *Protein Sci. 8*, 1536−45.
43. Adam, V., Royant, A., Niviere, V., Molina-Heredia, F. P., and Bourgeois, D. (2004) Structure of superoxide reductase bound to ferrocyanide and active site expansion upon X-ray-induced photoreduction, *Structure 12*, 1729−40.
44. deMare, F., Kurtz, D. M., Jr., and Nordlund, P. (1996) The structure of *Desulfovibrio vulgaris* rubrerythrin reveals a unique combination of rubredoxin-like FeS_4 and ferritin-like diiron domains, *Nat. Struct. Biol. 3*, 539−46.
45. Sieker, L. C., Holmes, M., Le Trong, I., Turley, S., Liu, M. Y., LeGall, J., and Stenkamp, R. E. (2000) The 1.9 Å crystal structure of the "as isolated" rubrerythrin from *Desulfovibrio vulgaris*: some surprising results, *J. Biol. Inorg. Chem. 5*, 505−13.
46. Li, M., Liu, M. Y., LeGall, J., Gui, L. L., Liao, J., Jiang, T., Zhang, J. P., Liang, D. C., and Chang, W. R. (2003) Crystal structure studies on rubrerythrin: enzymatic activity in relation to the zinc movement, *J. Biol. Inorg. Chem. 8*, 149−55.
47. Fushinobu, S., Shoun, H., and Wakagi, T. (2003) Crystal structure of sulerythrin, a rubrerythrin-like protein from a strictly aerobic archaeon, *Sulfolobus tokodaii* strain 7, shows unexpected domain swapping, *Biochemistry 42*, 11707−15.
48. Pierik, A. J., Wolbert, R. B., Portier, G. L., Verhagen, M. F., and Hagen, W. R. (1993) Nigerythrin and rubrerythrin from *Desulfovibrio vulgaris* each contain two mononuclear iron centers and two dinuclear iron clusters, *Eur. J. Biochem. 212*, 237−45.
49. Romao, C. V., Liu, M. Y., Le Gall, J., Gomes, C. M., Braga, V., Pacheco, I., Xavier, A. V., and Teixeira, M. (1999) The superoxide dismutase activity of desulfoferrodoxin from *Desulfovibrio desulfuricans* ATCC 27774, *Eur. J. Biochem. 261*, 438−43.
50. Moura, I., Tavares, P., Moura, J. J., Ravi, N., Huynh, B. H., Liu, M. Y., and LeGall, J. (1990) Purification and characterization of desulfoferrodoxin. A novel protein from *Desulfovibrio desulfuricans* (ATCC 27774) and from *Desulfovibrio vulgaris* (strain Hildenborough) that contains a distorted rubredoxin center and a mononuclear ferrous center, *J. Biol. Chem. 265*, 21596−602.
51. Jenney, F. E., Jr., Verhagen, M. F., Cui, X., and Adams, M. W. (1999) Anaerobic microbes: oxygen detoxification without superoxide dismutase, *Science 286*, 306−9.
52. Emerson, J. P., Cabelli, D. E., and Kurtz, D. M., Jr. (2003) An engineered two-iron superoxide reductase lacking the $[Fe(SCys)_4]$ site retains its catalytic properties in vitro and in vivo, *Proc. Natl. Acad. Sci. U.S.A. 100*, 3802−7.
53. Yeh, A. P., Hu, Y., Jenney, F. E., Jr., Adams, M. W., and Rees, D. C. (2000) Structures of the superoxide reductase from *Pyrococcus furiosus* in the oxidized and reduced states, *Biochemistry 39*, 2499−508.
54. Bugg, T. D. (2001) Oxygenases: mechanisms and structural motifs for O_2 activation, *Curr. Opin. Chem. Biol. 5*, 550−5.
55. Bugg, T. D., Sanvoisin, J., and Spence, E. L. (1997) Exploring the catalytic mechanism of the extradiol catechol dioxygenases, *Biochem. Soc. Trans. 25*, 81−5.
56. Lange, S. J., and Que, L., Jr. (1998) Oxygen activating nonheme iron enzymes, *Curr. Opin. Chem. Biol. 2*, 159−72.
57. Que, L., Jr., and Ho, R. Y. (1996) Dioxygen Activation by Enzymes with Mononuclear Non-Heme Iron Active Sites, *Chem. Rev. 96*, 2607−24.
58. Colabroy, K., and Begley, T. P. (2005) The pyridine ring of NAD is formed by a non-enzymatic pericyclic reaction, *J. Am. Chem. Soc. 117*, 840−1.
59. Sanvoisin, J., Langley, G. J., and Bugg, T. D. H. (1995) Mechanism of Extradiol Catechol Dioxygenases: Evidence for a Lactone Intermediate in the 2,3-Dihydroxyphenylpropionate 1,2-Dioxygenase Reaction, *J. Am. Chem. Soc. 117*, 7836−7.
60. Spence, E. L., Langley, G. J., and Bugg, T. D. H. (1996) Cis-Trans Isomerization of a Cyclopropyl Radical Trap Catalyzed by Extradiol Catechol Dioxygenases: Evidence for a Semiquinone Intermediate, *J. Am. Chem. Soc. 118*, 8336−8343.
61. Winfield, C. J., Al-Mahrizy, Z., Gravestock, M., and Bugg, T. D. H. (2000) Elucidation of the catalytic mechanisms of the non-haem iron-dependent catechol dioxygenases: synthesis of carba-analogues for hydroperoxide reaction intermediates, *Perkin 1*, 3277−89.
62. Mayer, R. J., and Que, L., Jr. (1984) Oxygen-18 studies of pyrogallol cleavage by catechol 1,2-dioxygenase, *J. Biol. Chem. 259*, 13056−60.
63. Vaillancourt, F. H., Barbosa, C. J., Spiro, T. G., Bolin, J. T., Blades, M. W., Turner, R. F., and Eltis, L. D. (2002) Definitive evidence for monoanionic binding of 2,3-dihydroxybiphenyl to 2,3-dihydroxybiphenyl 1,2-dioxygenase from UV resonance Raman spectroscopy, UV/Vis absorption spectroscopy, and crystallography, *J. Am. Chem. Soc. 124*, 2485−96.
64. Bugg, T. D. H., and Lin, G. (2001) Solving the riddle of the intradiol and extradiol catechol dioxygenases: how do enzymes control hydroperoxide rearrangements?, *Chem. Commun.*, 941−952.
65. Lin, G., Reid, G., and Bugg, T. D. (2001) Extradiol oxidative cleavage of catechols by ferrous and ferric complexes of 1,4,7-triazacyclononane: insight into the mechanism of the extradiol catechol dioxygenases, *J. Am. Chem. Soc. 123*, 5030−9.
66. Mendel, S., Arndt, A., and Bugg, T. D. H. (2004) Acid-Base Catalysis in the Extradiol Catechol Dioxygenase Reaction Mechanism: Site-Directed Mutagenesis of His-115 and His-179 in *Escherichia coli* 2,3-Dihydroxyphenylpropionate 1,2-Dioxygenase (MhpB), *Biochemistry 43*, 13390−6.

BI047353L